Design of Bismuth Tungstate Bi$_2$WO$_6$ Photocatalyst for Enhanced and Environmentally Friendly Organic Pollutant Degradation

Aicha El Aouni [1], Mohamed El Ouardi [1,2], Madjid Arab [2], Mohamed Saadi [1], Henrik Haspel [3,4], Zoltán Kónya [3,4], Abdelkader Ben Ali [1], Amane Jada [5,6], Amal BaQais [7] and Hassan Ait Ahsaine [1,*]

1   Laboratoire de Chimie Appliquée des Matériaux, Centre des Sciences des Matériaux, Faculty of Sciences, Mohammed V University, Rabat 1014, Morocco; aicha.elaouni@um5r.ac.ma (A.E.A.); mohamed.elouardi@um5r.ac.ma (M.E.O.); m.saadi@um5r.ac.ma (M.S.); a.benali@um5r.ac.ma (A.B.A.)
2   Aix Marseille University, Université de Toulon, CNRS, IM2NP, CS CEDEX 9, 60584 Toulon, France; madjid.arab@univ-tln.fr
3   HUN-REN-SZTE Reaction Kinetics and Surface Chemistry Research Group, Rerrich Béla tér 1, H-6720 Szeged, Hungary; haspel@chem.u-szeged.hu (H.H.); konya@chem.u-szeged.hu (Z.K.)
4   Department of Applied and Environmental Chemistry, University of Szeged, Rerrich Béla tér 1, H-6720 Szeged, Hungary
5   Institute of Materials Science of Mulhouse (IS2M), Haute Alsace University, 68100 Mulhouse, France; amane.jada@uha.fr
6   Strasbourg University, 67081 Strasbourg, France
7   Department of Chemistry, College of Science, Princess Nourah Bint Abdulrahman University, P.O. Box 84428, Riyadh 11671, Saudi Arabia; aabaqeis@pnu.edu.sa
*   Correspondence: h.aitahsaine@um5r.ac.ma

Abstract: In this study, a chemical precipitation approach was adopted to produce a photocatalyst based on bismuth tungstate Bi$_2$WO$_6$ for enhanced and environmentally friendly organic pollutant degradation. Various tools such as X-ray diffraction (XRD), Raman spectroscopy, scanning electron microscopy (SEM), optical spectroscopy and X-ray photoelectron spectroscopy, were employed to assess the structural and morphological properties. Hence, the XRD profiles showed a well crystallized Bi$_2$WO$_6$ orthorhombic phase. The photocatalytic performance of the resulting photocatalyst was assessed by the decomposition of Rhodamine B (RhB) and methyl orange (MO) with a decomposition efficiency of 97 and 92%, along with the highest chemical oxygen demand of 82 and 79% during 120 min of illumination, respectively. The principal novelty of the present work is to focus on the changes in the crystalline structure, the morphology, and the optical and the photoelectrochemical characteristics of the Bi$_2$WO$_6$, by tuning the annealing temperature of the designed photocatalyst. Such physicochemical property changes in the as-prepared photocatalyst will affect in turn its photocatalytic activity toward the organic pollutant decomposition. The photocatalytic mechanism was elaborated based on electrochemical impedance spectroscopy, photocurrent analysis, photoluminescence spectroscopy, and radical trapping measurements. The overall data indicate that the superoxide O$_2^{\bullet-}$ and holes h$^+$ are the principal species responsible for the pollutant photodegradation.

Keywords: bismuth tungstate; photocatalysis; degradation mechanism; active species

1. Introduction

With the global advancement of urbanization, economy, and industry, various domestic activities and industrial discharges are generating a wide range of pollutants. These pollutants have high bioconcentration capacities in the environment, leading to severe atmospheric damage and negative impacts on all life forms [1–7]. Mainly, the discovery of the photocatalytic phenomenon in 1969 opened up new avenues for effectively decontaminating air, water, and soil through extensive research [8–13]. Consequently,

significant research efforts have been channeled toward investigating the reaction between complex dye pollutants and various disinfectants. Various advanced oxidation technologies have been engineered to achieve environmentally friendly pollutant removal, including adsorption [14–17], electrocatalytic degradation [18–20], and photodegradation [21–23]. The ultimate goal is to degrade these organic contaminants into harmless substances like H_2O and CO_2 [24–26]. To achieve this, researchers have focused on developing innovative photocatalysis methods, particularly utilizing common photocatalysts with wider energy bandgaps, including oxides with diverse crystalline structures [27]. However, more recent studies have been focused on the creation of new visible-light-induced photocatalysts. Some of the materials currently under investigation include semiconductor oxides like $NaTaO_3$ [28], $CaIn_2O_4$ [29], γ-Bi_2MoO_6 [30], $Bi_4Ti_3O_{12}$ [31], and Bi_2WO_6 [32]. These materials offer a promising way to advance the area of photocatalysis and its potential for environmentally friendly pollutant degradation.

Among numerous visible-light-driven photocatalysts, Bismuth tungstate (Bi_2WO_6) has garnered considerable interest within the scientific community thanks to its distinctive optical, electronic, and photocatalytic characteristics [33,34]. Its structural composition contains interconnected layers of $[Bi_2O_2]^{2+}$ and WO_6 octahedra [23]. This layered configuration of Bi_2WO_6 offers advantages in promoting charge transfer and minimizing the recombination of photo-generated electron-hole charges, which are crucial processes in photocatalysis and other photoactive applications [35–37]. Thus, with a band gap of 2.8 eV, Bi_2WO_6 exhibits a propensity for absorbing in an extended wavelength region. This results in high efficiency in breaking down pollutants upon exposure to visible light, making it particularly suitable for solar energy-driven environmental remediation, such as water purification and air treatment [18,19]. In order to widen the visible light absorption and enhance the photocatalytic performance of Bi_2WO_6, different methods have been proposed. For instance, high-quality Bi_2WO_6 nanoparticles (NPs) were obtained via hydrothermal approaches [38], sol-gel procedures [39], microwave synthesis [40], chemical precipitation [41], and solvothermal methods [42].

In the present work, to design Bi_2WO_6 nanoparticles (BWO), we have used the traditional chemical precipitation method, due to its simple, inexpensive, and surfactant-free attributes. Thereafter, the as-prepared samples were calcined at 400 °C, 500 °C, and 600 °C in order to investigate the effect of calcination temperature on the structure and properties of the resulting materials. Various analytical techniques including powder X-ray diffraction (XRD), scanning electron microscopy (SEM), Raman spectroscopy, X-ray photoelectron spectroscopy (XPS), UV-vis diffuse reflectance spectroscopy (DRS), and photoluminescence spectroscopy (PL) were employed to assess the structural, morphological, and optical characteristics of the prepared materials. Further, the effects of the designed photocatalyst calcination on its crystalline properties, its morphology, and its pollutant removal efficiencies were systematically examined. The photodegradation performance was evaluated by RhB and MO dye-removing ability in an aqueous medium under irradiation with visible light. Additionally, we investigated the active species engaged in the breakdown of RhB over the Bi_2WO_6 and assessed the cycling performance of the catalyst as well.

2. Experimental Section

2.1. BWO Synthesis

All chemicals employed here were of analytical grade from Sigma-Aldrich, and were processed directly without further purification. Typically, Sodium tungstate dehydrate [$Na_2WO_4 \cdot 2H_2O$], bismuth nitrate pentahydrate [$Bi(NO_3)_3 \cdot 5H_2O$], nitric acid (HNO_3), and ammonium hydroxide (NH_4OH) were used as precursors.

Initially, $Bi(NO_3)_3 \cdot 5H_2O$ was solubilized in a volume of diluted HNO_3 (10%, v/v) solution at 25 °C. The resulting nitrate solution was then dropped into 0.1 L of aqueous $Na_2WO_4 \cdot 2H_2O$ solution under vigorous stirring for 2 h. The pH was set to pH = 5.5 by introducing NH_4OH to the solution, which was then placed in a condenser surrounded by an oil bath under continuous agitation. The solution temperature was kept between 70

and 80 °C for 24 h. The obtained white precipitate was isolated by centrifugation, washed repeatedly with distilled water and finally dried in an oven. Part of the as-prepared BWO powder was subjected to calcination in a tube furnace at 400 °C, 500 °C, and 600 °C for 3 h under flowing argon atmosphere.

2.2. Material Characterization

The BWO powder was structurally investigated by XRD using an EMPYREAN Panalytical (Toulon University France) diffractometer mounted with a copper X-ray source (wavelength λ = 1.5440 Å) and a Ni filter to eliminate K_β radiation. The 2Θ range of 10–80° was scanned with a step size of 0.026°. Raman spectroscopy was employed to characterize the vibrational properties of the obtained materials. The Raman profile was acquired by a JASCO (Toulon University, France) spectrometer operated with a 633 nm laser. The BWO grain morphology was examined by scanning electron microscopy (SEM) (Thermo-Fisher Scientific Apreo C, Szeged, Hungary) equipped with a Röntec QXE energy dispersive X-ray spectrometer. The survey and high-resolution XPS spectra were performed by X-ray photoelectron spectroscopy (XPS) by using a (Mulhouse, France) coupled with a concentric hemi-spherical analyzer. To determine the absorption range and band gap energy of BWO, the absorption profile was recorded in the 200–800 nm wavelength interval using an ultraviolet-visible spectrophotometer (JASCO UV-Vis V-730). Photoluminescence (PL) measurements were registered using a Fluoromax fluorescence spectrophotometer (Horiba, Toulon, France).

2.3. Photocatalytic Procedure

A representative photocatalytic RhB and MO decomposition measurement was as follows. A total of 100 mg of BWO was solubilized in 100 mL RhB and MO solutions (5 ppm) and the pH of the suspensions was set to pH = 5.5 and 5.8, respectively. After ultrasonication for 10 min, the resulting suspensions were agitated in the dark for an additional 2 h to achieve adsorption–desorption equilibrium between BWO and the dyes. The mixture was illuminated with a Philips lamp (tungsten lamp 300 W), while being continuously stirred. At specific time intervals, 3 mL of the solution was withdrawn and centrifuged at 13,400 rpm for 10 min to eliminate the BWO from the suspension. The evolutions of MO and RhB decomposition were studied using a Shimadzu (Kyoto, Japan) UV 2600 spectrophotometer by measuring the aqueous solution absorbance in the 400–800 nm wavelength region. To confirm the radicals produced by the BWO under irradiation and responsible for the photocatalytic activity, a series of scavenger tests was conducted. Thus, chemical scavengers such as Ethylene Diamine disodium Tetra-Acetate (EDTA), Isopropanol (IPA), and L-ascorbic acid, were selected to trap the active species h^+, $OH^\bullet$, and $O_2^{\bullet-}$, respectively.

2.4. Measurement of Zero Charge Point

The point of zero charge (pH_{pzc}) can be described as the pH where the charges resulting from negative and positive surface groups are equal. The pH_{pzc} of the BWO surface was obtained by the method proposed by Al-Harahsheh [43]. Thus, a sample amount of 0.05 g was transferred to six beakers filled with 50 mL of 0.1 M potassium nitrate (KNO_3) solution. To obtain the curve of the zero-point charge measurements, the initial pH values of the beakers were set at to 2.2, 4.3, 6.1, 8.2, 10.4, and 12.1 by adding some drops of 0.1 M HNO_3 or 0.1 M NaOH. The obtained suspensions were left to equilibrate for one day. After filtration, the final pHs were measured.

2.5. Photoelectrochemical Measurement

Photoelectrochemical analyses were undertaken using an OrigaLys ElectroChem (Rillieux-La-Pape, France) electrochemical workstation in a three-electrode configuration. Ag/AgCl and platinum foil were chosen as reference and counter electrodes, respectively. Sample-coated indium tin oxide (ITO) substrates were used as working electrodes (WE) in

0.1 M sodium sulfate (Na_2SO_4) aqueous electrolyte. The visible light source was a 300 W Xe lamp fitted with a 420 nm cut-off filter (λ > 420 nm). The WE was fabricated on ITO glass by drop casting. In a typical deposition, ITO glass slides were cleaned with acetone and ethanol. To prepare the electrode, a mass of 10 mg of photocatalyst powder was mixed with 2 mL of absolute ethanol by ultra-sonication for 15 min to form a well-dispersed suspension. Afterward, 100 µL of the suspension was dropped onto a 1×1 cm^2 ITO substrate and dried at 100 °C for 5 h. The transient photocurrent was measured under 0.5 V bias. Electrochemical impedance spectra (EIS) were recorded in the 0.01–10^5 Hz frequency range using an amplitude of 5 mV, while Mott–Schottky graphs were constructed at a frequency of 500 Hz.

2.6. Chemical Oxygen Demand (COD)

The mineralization of the cationic dye (RhB) and anionic dye (MO) during photocatalytic reaction has been assessed through measuring the chemical oxygen demand (*COD*). RhB and MO photodecomposition tests were conducted in a 100 mL beaker at ambient temperature. The *COD* was measured by using a Lovibond *COD* kit (Dortmund, Germany), and the results were obtained using an MD 200 *COD* spectrophotometer. The rate of photodecomposition was defined as COD_t/COD_0 vs. time. The rate was computed for different photocatalytic reaction times according to the following equation:

$$COD(\%) = \left(\frac{COD_0 - COD_t}{COD_0} \right) \times 100 \tag{1}$$

COD_0: *COD* content (mg/L of O_2) before decomposition.
COD_t: *COD* content (mg/L of O_2) at a time t.

3. Results and Discussion

3.1. Structural Investigation

The diffraction profiles of BWO NPs annealed at 400, 500, and 600 °C are presented in Figure 1. As shown in the figure, all peaks in the XRD profiles are in good conformity with the JCPDS card No. 01-079-2381 and correspond to the pure BWO orthorhombic phase. The determination of grain size involved the application of the Scherer formula, leading to grain sizes of 14, 24, and 28 nm for the BWO NPs after calcination at temperatures of 400, 500, and 600 °C, respectively. Meanwhile, the lattice parameters and unit cell volumes of the BWO NPs after calcination at varying temperatures were determined using the following equations.

$$\frac{1}{d_{hkl}^2} = \frac{h^2}{a^2} + \frac{k^2}{b^2} + \frac{l^2}{C^2} \tag{2}$$

$$V = abc \tag{3}$$

The results for calcined BWO NPs are shown in Table 1 and reveal a close alignment between the experimental findings and the established reference values for orthorhombic BWO. Moreover, as the treatment temperature increases, differences emerge in the response of the crystal lattice along its distinct axes. These variations can be attributed to the material's propensity for structural phase transitions at varying temperature levels. Consequently, a significant augmentation in grain size is observed, likely attributable to the process of recrystallization and the aggregation of ultrafine grains.
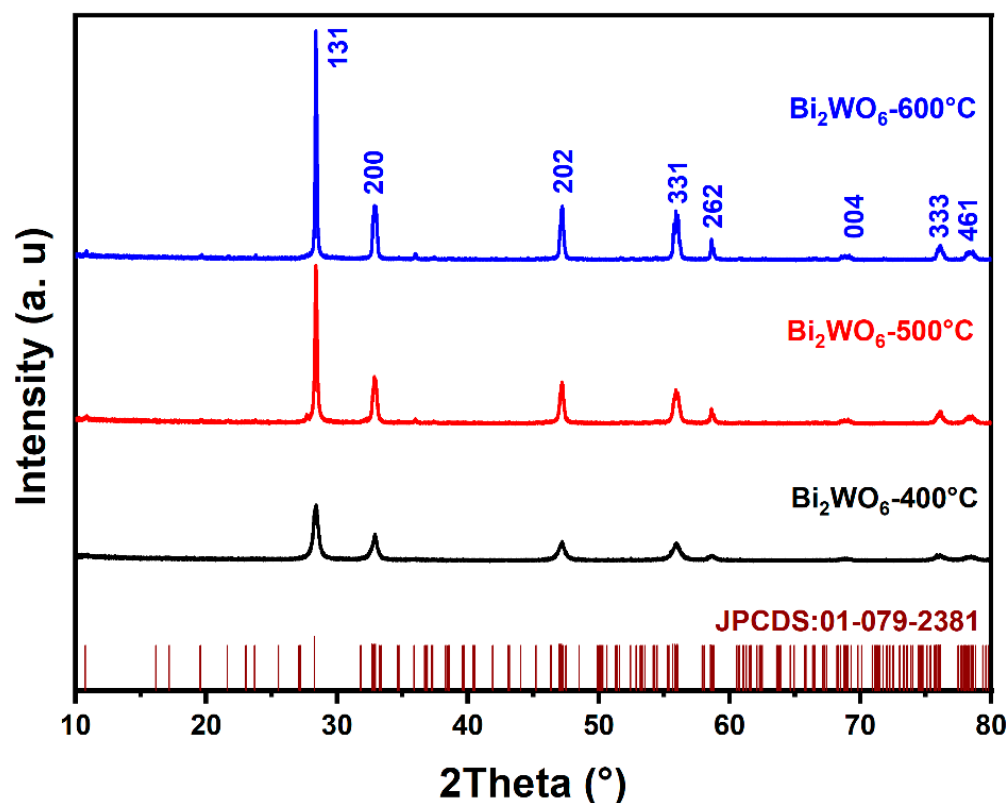
Figure 1. XRD patterns of BWO NPs annealed at 400, 500, and 600 °C.

Table 1. Lattice parameters and volume of the unit cell of BWO NPs calcined at 400, 500, and 600 °C.

Treatment Temperature	a (Å)	b (Å)	c (Å)	Unit Cell Volume (Å)^3
JCPDS card No. 01-079-2381	5.4373	16.4302	5.4584	487.6312
400 °C	5.4430	16.3134	5.4486	483.8021
500 °C	5.4428	16.3141	5.4474	483.6985
600 °C	5.4419	16.3204	5.4457	483.6543

3.2. Vibrational Spectroscopy

The experimental Raman spectra of Bi_2WO_6 with characteristic peaks in the wavenumber region of 110 to 1200 cm^{-1} at various temperatures are presented in Figure 2. The BWO400, BWO500, and BWO600 samples show the characteristic Raman peaks of Bi_2WO_6. The Raman strong peaks at 818 cm^{-1} and 794 cm^{-1} corresponded to the symmetric and antisymmetric A_g modes of terminal O–W–O, respectively. Changes in calcination temperature result in alterations in the shape and position of the O–W–O vibration bands, with the 794 cm^{-1} band shifting to lower wavenumbers and the 818 cm^{-1} band shifting to higher wavenumbers [44]. Additionally, the presence of a peak at 724 cm^{-1} signifies the tungstate chain's antisymmetric bridging mode, with its wavenumber decreasing as the calcination temperature decreases [45]. Moreover, the peak at 310 cm^{-1} is ascribed to the translation mode due to the simultaneous movements of Bi^{3+} and WO_6, while the 154 cm^{-1} peak relates to external vibrations of the WO_6 octahedron. Peaks observed between 200 and 520 cm^{-1} primarily arise from bending vibrations or stretching of the Bi–O bonds, BiO_6 polyhedron, and WO_6 octahedron [46].
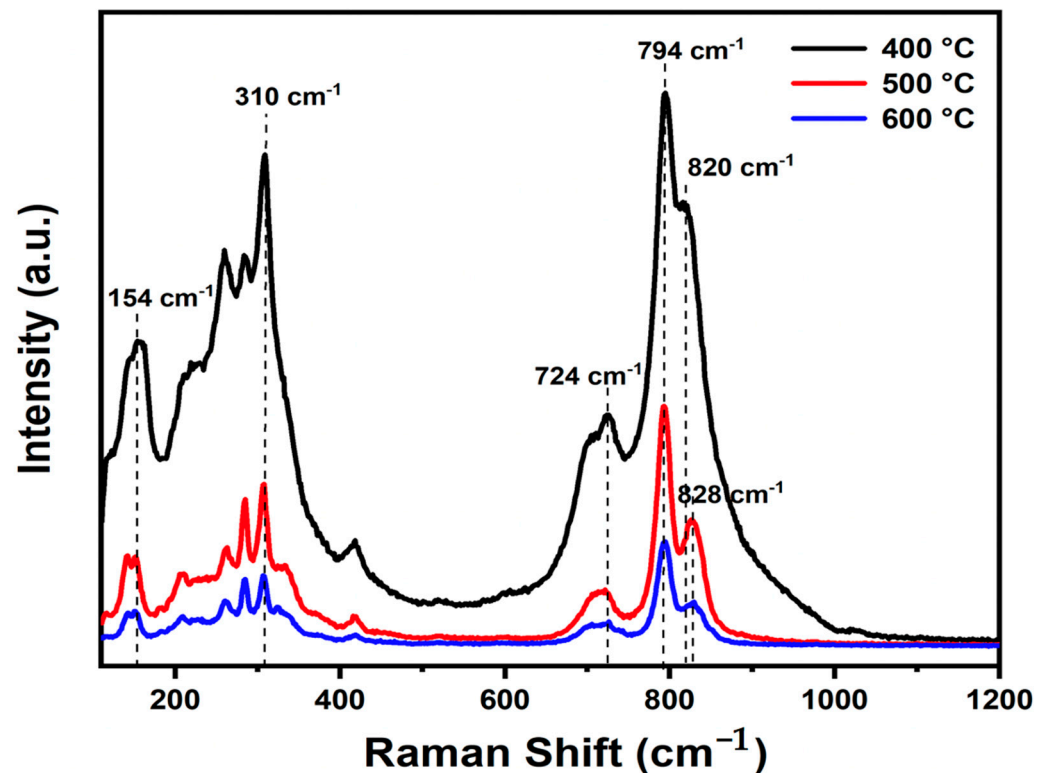
Figure 2. Raman spectra of the BWO NPs calcined at 400, 500, and 600 °C.

The peaks are arranged linearly at 820 cm^{-1} and 828 cm^{-1}, indicating a clear distortion in bond length with temperature of calcination. The O–W–O bond length of the samples was determined according to the given formula [47].

$$\nu\left(\text{cm}^{-1}\right) = 21,349 \cdot e^{[1.917 \cdot R(\text{Å})]} \tag{4}$$

where R is the bond length (Å) and ν is the Raman stretching frequency (cm^{-1}). The computed bond lengths for the studied BWO samples are given in Table 2.

Table 2. Frequency of the symmetric A_g modes of the terminal O–W–O stretching vibration and corresponding bond lengths for samples calcined at 400, 500, and 600 °C.

Treatment Temperature	Raman Stretching Frequency (cm^{-1})	Bond Length (Å)
400 °C	820	1.7003
500 °C	828	1.6952
600 °C	828	1.6852

Furthermore, it is noteworthy that the Raman peaks of BWO-500 and BWO-600 show decreased intensity and increased width in comparison to BWO-400. This change in bond length could potentially be ascribed to the recrystallization of BWO NPs at elevated calcination temperatures.

3.3. Morphology Analysis

The scanning electron microscopy (SEM) analyses are presented in Figure 3 and provide insights into the morphology of BWO NPs, enabling the observation of variations in particle size and shape resulting from different calcination temperatures. At all three calcination temperatures, Figure 3a,d correspond to a calcination temperature of 400 °C, Figure 3b,e to 500 °C, and Figure 3c,f to 600 °C. The morphology reveals the presence of uniformly spherical particles. Notably, the size distribution of these particles at 400,

500, and 600 °C measures less than 1 μm. Additionally, it is obvious that the BWO NPs size increases progressively with higher calcination temperatures, aligning well with the findings of X-ray diffraction analysis. This observed rise in particle size can be explained by the agglomeration of nanoparticles that occurs at elevated calcination temperatures. SEM-mapping and EDS spectra were conducted to study the elements' distribution across the particle surface, as illustrated in Figure 3g–k. The results demonstrate a relatively consistent distribution of O, W, and Bi elements on the surface of the sample particles. These observations align well with the findings from Raman and XRD analyses.
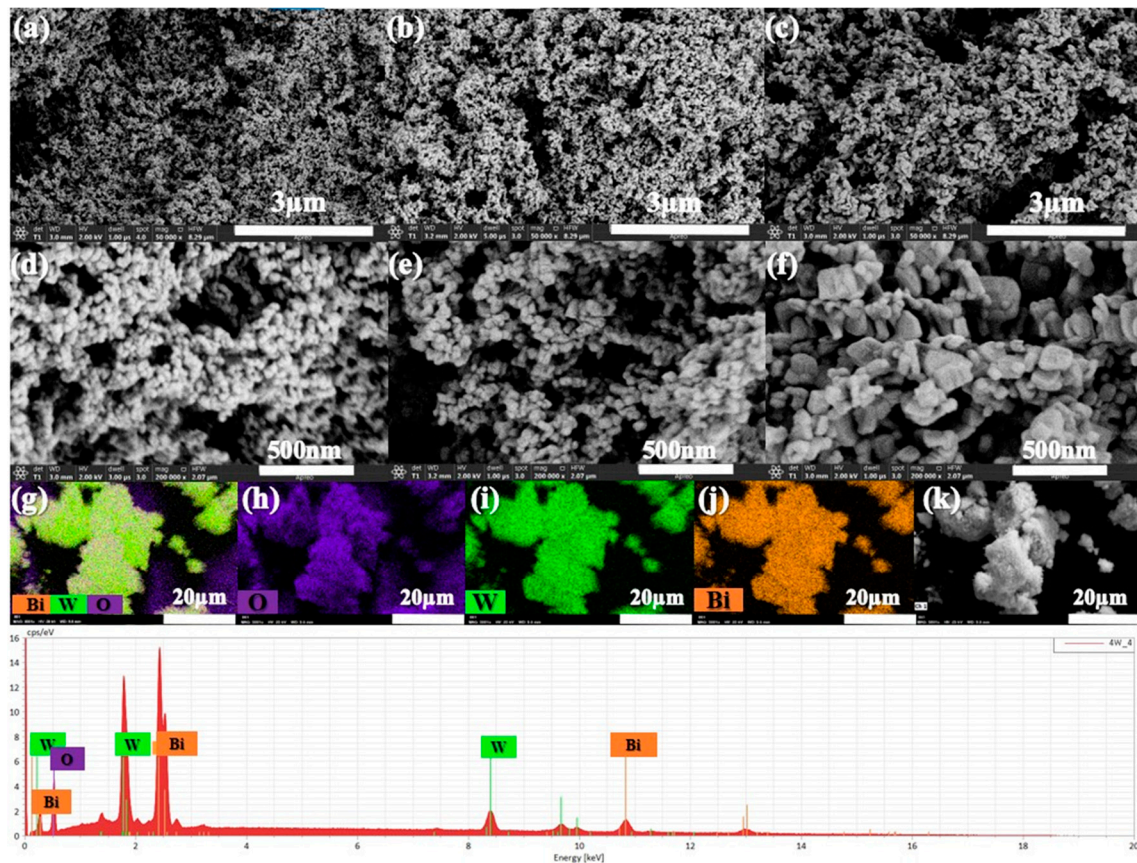

Figure 3. SEM analysis of the BWO NPs synthesized at 400 °C (**a**,**d**), 500 °C (**b**,**e**), 600 °C (**c**,**f**), and the elemental mapping (EDS) images (**g**–**k**) of BWO400.

3.4. Optical Properties

UV-vis diffuse reflectance spectroscopy was employed to explore the annealing temperature effect on the optical characteristics of the catalysts and to derive their bandgap energy (E_g) values. Figure 4a displays the diffuse reflectance graph of BWO with excellent optical absorption and shows that the absorption of light is enhanced as the annealing temperature decreases. The bandgap energy (E_g) was determined from Tauc's equation, $(\alpha h\nu)^{1/\gamma} = B (h\nu - E_g)$ [48], in which ν: photon frequency, α: absorption coefficient, h: Planck's constant, and γ: coefficient = 2 or 1/2 for both indirect and direct band gaps. Several investigations have shown that BWO has a direct band gap [49,50].

The resulting E_g values were found to be 2.87, 2.95, and 2.97 eV for BWO400, BWO500, and BWO600, respectively (Figure 4b).
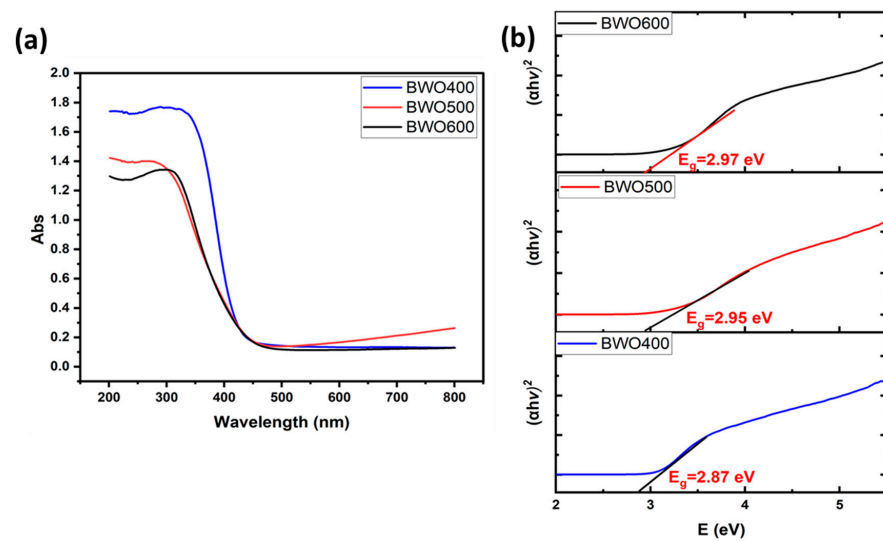
Figure 4. UV-visible diffuse reflectance graph of BWO NPs annealed at 400, 500, 600 °C (**a**), and their corresponding Tauc plots with band gap energies indicated (**b**).

3.5. X-ray Photoelectron Spectroscopy (XPS)

X-ray photoelectron spectroscopy (XPS) was also employed to determine the chemical states and surface chemical composition of the BWO400. Figure 5a presents the survey spectrum of the BWO400 material composed of W, Bi, and O elements and a little carbon trace. The existence of carbon can be explained by the use of a carbon tape within the XPS analysis [51]. Figure 5b shows the spin-orbit components of Bi 4f by two intense peaks found at 164.41 and 159.14 eV, assigned to the $4f_{5/2}$ and $4f_{7/2}$ states of the Bi^{3+} crystal structure, respectively [51]. Another spin-orbit doublet at 162.10 and 156.76 eV for Bi $4f_{5/2}$ and Bi $4f_{5/2}$ was also seen, respectively [52]. The peaks at 35.5 and 37.6 eV, as illustrated in Figure 5c, equivalent to W $4f_{7/2}$ and W $4f_{5/2}$, respectively, may be ascribed to a W^{6+} oxidation state [51,53,54]. Figure 5d reveals the existence of an oxygen element (O1s) via the clear, strong peak at 530.1 eV, which is assigned to the crystal lattice oxygen [55].
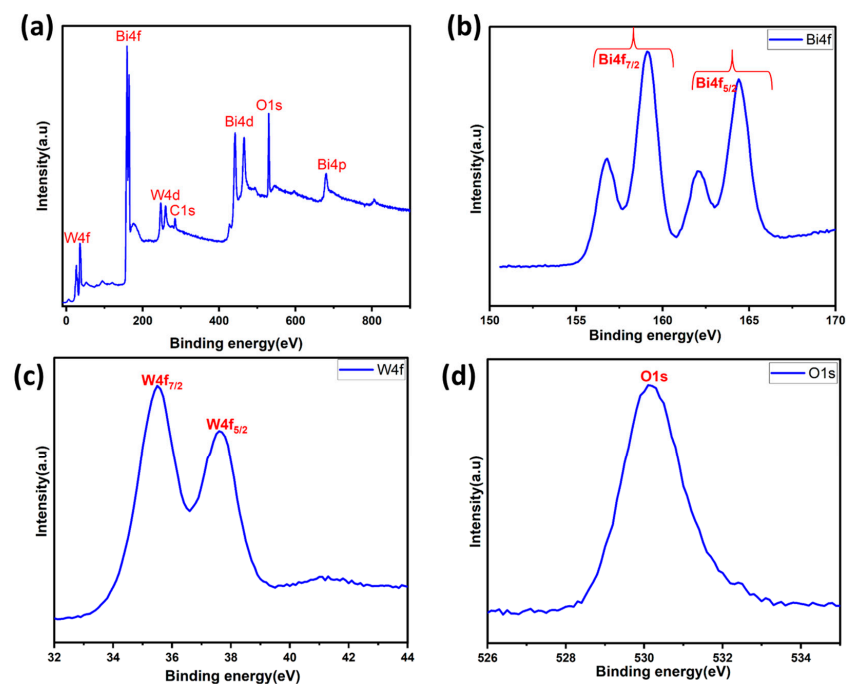

Figure 5. XPS survey (**a**) and high-resolution spectra of the BWO400 photocatalyst: Bi 4f (**b**), W 4f (**c**), and O 1s (**d**).

4. Assessment of the Photocatalytic Performance of BWO Photocatalyst

4.1. Adsorption and Photolysis Investigation

To prove the capability of our BWO400 material, it is important to study the adsorption of the pollutant in the absence of UV-vis illumination. Hence, the photolysis test enables the quantification of the photocatalytic decomposition contribution under our running parameters. Therefore, preliminary investigations were undertaken to check the contribution of the adsorption and the photolysis to the removal of the pollutant (case of RhB and MO). Figure 6a,b show the absorption curves of RhB (554 nm) and MO (463 nm) in the presence of BWO400 photocatalyst and in the absence of irradiation. It can be easily seen that the decline in the absorbance intensity of the highest RhB absorption bands is not more than 9% after 2 h of contact (Figure 6a), whereas in the MO it was 10.8% after 2 h of contact (Figure 6b). These results indicate very little adsorption of RhB and MO by the BWO400 material. The photolysis tests (absence of BWO400) were carried out on solutions (MO and RhB) with an initial dye concentration of 5 ppm under UV-vis illumination. Figure 6c,d reveal that in the absence of the BWO400 photocatalyst, only a reduction of 5% and 4% in the absorbance intensities was achieved after 2 h of illumination for RhB and MO, respectively. From these findings, we are able to confirm that the major process implicated in the removal of MO and RhB in the presence of BWO400 photocatalyst is principally photocatalytic decomposition instead of adsorption and photolysis processes.
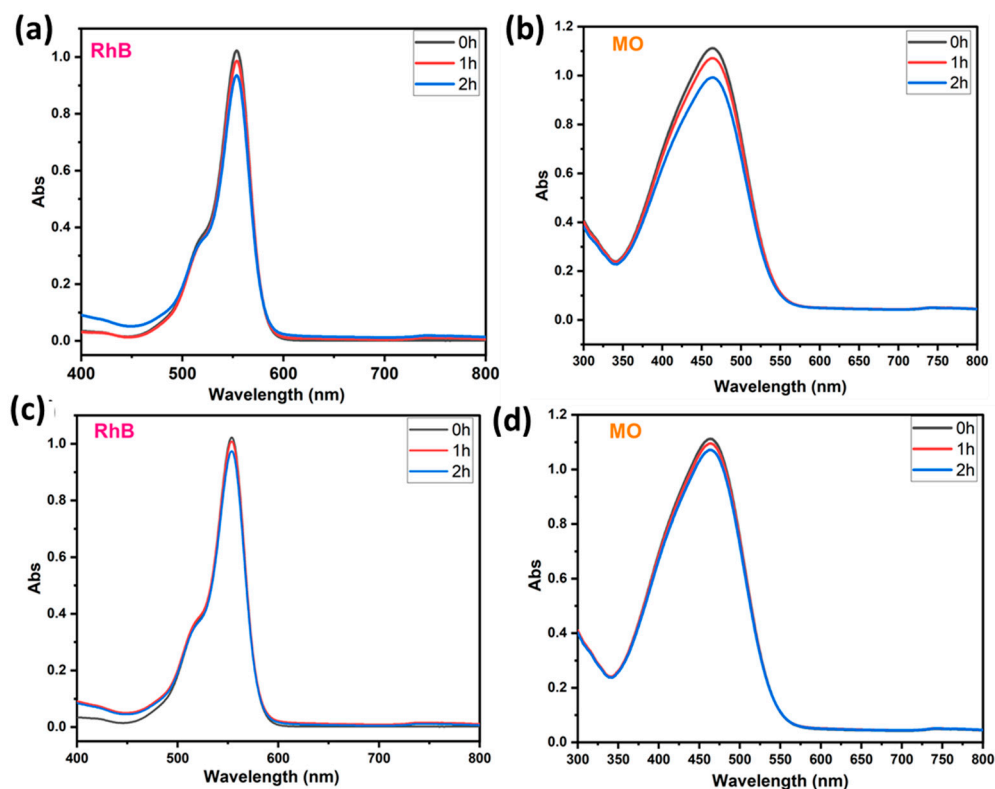

Figure 6. Visible absorption spectra of RhB and MO in the presence of BWO400 and in the absence of light (**a**,**b**); RhB and MO removal under illumination in the absence of BWO400 (**c**,**d**).

4.2. Photocatalytic Activity and Kinetic Investigation of BWO

4.2.1. The Case of Rhodamine B

The photocatalytic performance of BWO treated at 400, 500, and 600 °C is assessed by the breakdwon of RhB dye molecules under light illumination. The photocatalytic dye decomposition efficiency curves of BWO calcined at several temperatures are illustrated in Figure 7a–d. For low concentrations (ppm), the Beer–Lambert law is applicable, so that the concentration is proportional to the absorbance. The photodecomposition efficacy was quantified by the ratios C_t/C_0 (Figure 7b), where C_t and C_0 are the concentrations of BWO

at times t and $t = 0$, respectively. To evaluate the kinetic constant (Figure 7c,d), which describes the photocatalytic efficacy, a first-order kinetic rate law (Langmuir–Hinshelwood model) was used:
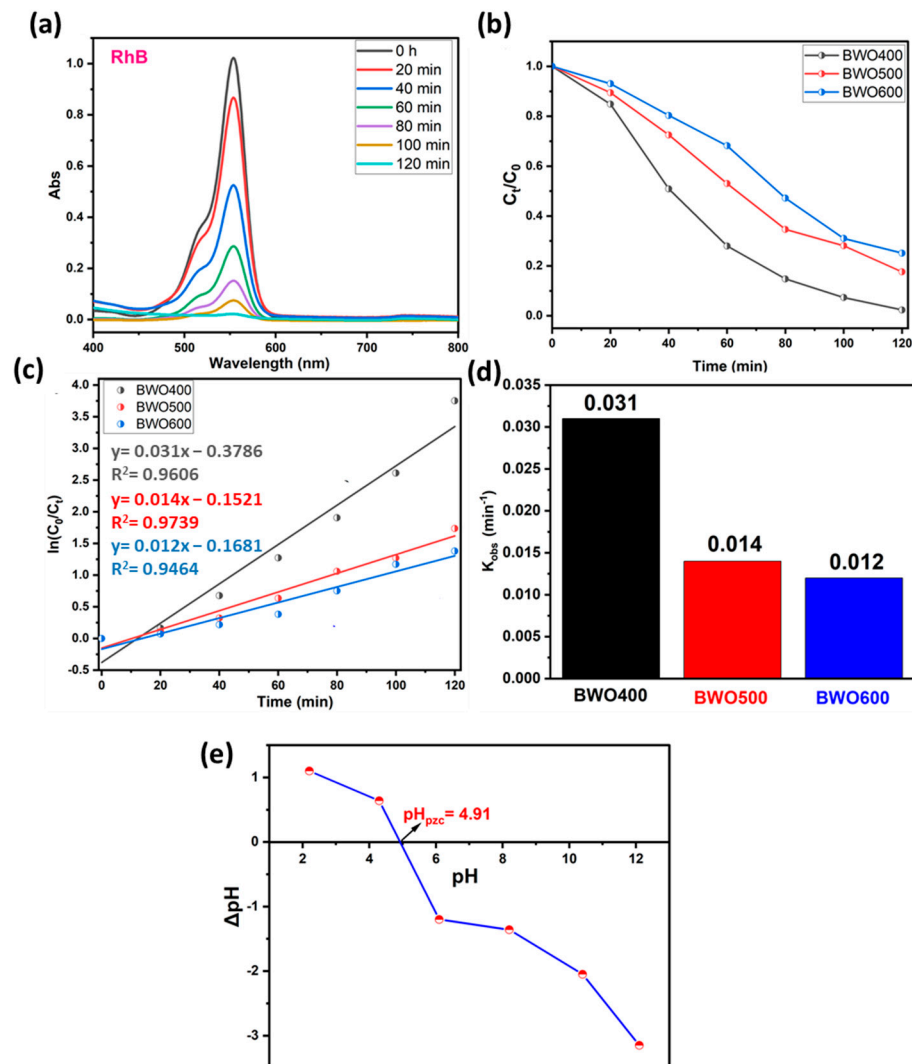
$$ln\frac{c_t}{c_0} = -k_{obs} \cdot t \tag{5}$$

Figure 7. UV-vis absorption spectra of RhB under solar light illumination on BWO400 (**a**), the variation of C_t/C_0 with illumination time on BWO400, BWO500, and BWO600 (**b**), fitted pseudo-first-order kinetics for the photodecomposition reaction along with the corresponding rate constants (**c**,**d**), and the identification of point of zero charge (pH$_{pzc}$) of BWO400 (**e**).

Figure 7a reveals that under UV illumination, the intensity of the contaminant absorption band declines with illumination time in the presence of BWO manufactured by co-precipitation method and heat-treated at 400 °C. Figure 7b illustrates the kinetics of photocatalytic decomposition in the presence of the different photocatalysts. More specifically, BWO calcined at 400 °C exhibited superior photocatalytic activity with 97% decomposition achieved within 120 min. This displays a better decomposition efficiency when compared to the BWO treated at 500 °C (82%) and 600 °C (75%). The results in Figure 7c demonstrate that the photocatalytic reaction obeys a pseudo-first-order kinetic rate law. The obtained rate constants k_{obs} are given in Figure 7d. Their values are 0.031, 0.014, and 0.012 min^{-1} for the BWO400, BWO500, and BWO600 photocatalysts, respectively. The decline in photocatalytic activity when the calcination temperature increases is ascribed to the quick recombination of photo-induced electrons and holes. Moreover, the optical properties of

BWO400, in particular its outstanding absorption of visible light and its low gap energy, encouraged us to adopt a lamp similar to solar illumination. In addition, this high efficiency of the BWO400 photocatalyst is also ascribed to the specific shape, featuring small, highly crystallized grains of the orthorhombic phase. It is worth mentioning that the as-produced material at this temperature presents good photocatalytic properties by delivering small particle size and more available surface sites for charge transfer [22,56]. These findings are consistent with XRD and SEM findings. To better understand and explain the mechanism behind the photocatalytic decomposition efficacy of RhB, we have measured the pH_{pzc} (Figure 7e). The pH_{pzc} is dependent on the acid-base characteristics of the surface material [25,57]. In this study, the orthorhombic BWO has a pH_{pzc} value equal to 4.91, and RhB is a cationic pollutant. At pH_i below or above pH_{pzc}, the surface charge of BWO is negative or positive, respectively. This implies that the surfaces of BWO may be negatively or positively charged depending on the aqueous phase pH. In our system, the pH of our system was 5.5, which is greater than pH_{pzc}, so BWO is negatively charged. As a result, the degradation efficiency is high owing to the electrostatic attraction occurring between the negatively charged catalyst surface and the positively charged cationic dye molecules. In addition, under alkaline media, photodegradation performance is more significant given the availability of hydroxyl ions, required for the creation of hydroxyl radicals.

4.2.2. The Case of Methyl Orange

To ensure the photocatalytic performance of BWO prepared at various calcination temperatures, another experiment was carried out on the decomposition of an organic dye like methyl orange (anionic dye). Figure 8a reveals that under UV illumination, the intensity of the contaminant absorption band (465 nm) declines with illumination time in the presence of BWO as prepared by the co-precipitation method and thermally treated at 400 °C. In addition, Figure 8b shows plots describing the variation in C_t/C_0 of the MO versus illumination time for the different photocatalysts (BWO400, BWO500, and BWO600). Similar to RhB, the results obtained for MO show that the degradation efficiency decreases with the switch from BWO400 to BWO600. In particular, the BWO treated at 400 °C displayed superior photocatalytic performance, with a decomposition efficacy of 92% in 120 min, while the BWO500 presented an efficiency of 78%, and the decomposition efficiency for the BWO600 was 70% during 120 min of irradiation. Figure 8c indicates that the photocatalytic reaction obeys a pseudo-first-order kinetic. The determined rate constants k_{obs} are given in Figure 8d. Their values are 0.0209, 0.0124, and 0.0097 min^{-1} for the BWO400, BWO500, and BWO600 photocatalysts, respectively. In addition to the optical characteristics, especially the gap energy and the PL readings, which show that BWO400 is more favorable for the degradation of MO, the achievement of this degradation efficiency (92%) can also be explained by the surface charge. In our reaction medium, the pH of our system is around 5.8, which is above pH_{pzc} (Figure 7e), so the BWO is negatively charged leading to a repulsion between the negatively charged MO molecules and the negatively charged BWO. This will result in a decrease in the pH of the medium toward a pH value lower than the pH_{pzc} and consequently the surface charge of BWO400 becomes positive. Consequently, the decomposing process is highly efficient owing to the electrostatic attraction occurring between the positively charged surface of the catalyst and the negatively charged dye molecule.
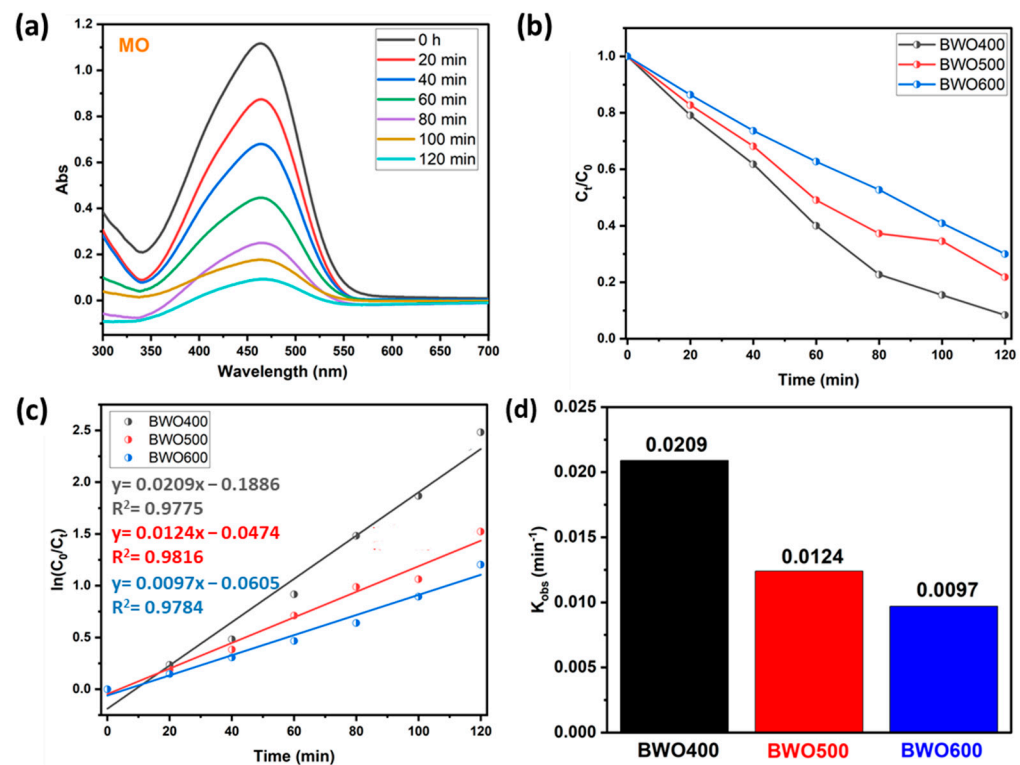
Figure 8. UV-vis absorption curve of MO under solar light illumination on BWO400 (**a**), the variation of C_t/C_0 with illumination time on BWO400, BWO500, and BWO600 (**b**), fitted pseudo-first-order kinetics for the photodecomposition (**c**), and corresponding rate constant of the photocatalytic reaction (**d**).

4.3. Investigation of the Photocatalytic Mechanism

The separation efficacy of the photo-induced charges is an essential parameter influencing the photocatalytic activity. To gain a better understanding of the mechanism of photocatalytic performance improvement, photoelectrochemical measurements and photoluminescence (PL) profiles were performed to characterize the separation behavior of the photo-induced charge. Figure 9a presents the transient photocurrent graphs of BWO400, BWO500, and BWO600. As shown, the photocurrent response of BWO400 is obviously greater than that of BWO500 and BWO600. The improved photocurrent density in BWO400 photocatalyst compared to BWO500 and BWO 600 is equivalent to a facilitated separation efficacy of the charge carriers, which greatly assists in improving the photocatalytic activity. It is interesting to note that the stable photocurrent density indicates good photoelectrochemical stability. In addition, Figure 9b displays the EIS Nyquist plots to examine the charge transfer characteristics of the as-prepared materials. It is widely known that the lower value of the arc radius is attributed to the quicker charge transfer rate and lower charge transfer resistance (R_{ct}) [58–61]. It can be clearly seen that BWO400 exhibits a smaller arc radius when compared to BWO500 and BWO600, which indicates that BWO400 exhibits the quickest charge transfer rate and the highest effective separation efficacy, which is in close correlation with the transient photocurrent response findings. From the PL curve (Figure 9c) of the obtained photocatalysts, a higher PL intensity is clearly found in BWO600 in comparison with BWO500 and BWO400, which confirms that the enhanced transport and separation of the photo-generated charge is obtained by decreasing the calcination temperature. Furthermore, BWO400 displays the lowest PL intensity of all the prepared photocatalysts, reflecting the substantial increase in charge separation efficiency. Spectroscopic and photoelectrochemical investigations clearly reveal that the efficacy of photo-induced charge, migration, and separation is considerably boosted by lowering the heat treatment temperature. By reducing the temperature, damaging or denaturing the active sites may be avoided, allowing the photocatalyst to keep its catalytic

activity. In addition, calcining at lower temperatures could lead to a band gap better adapted to the uptake of visible light. This enhanced absorption of light could improve photocatalytic activity [62].
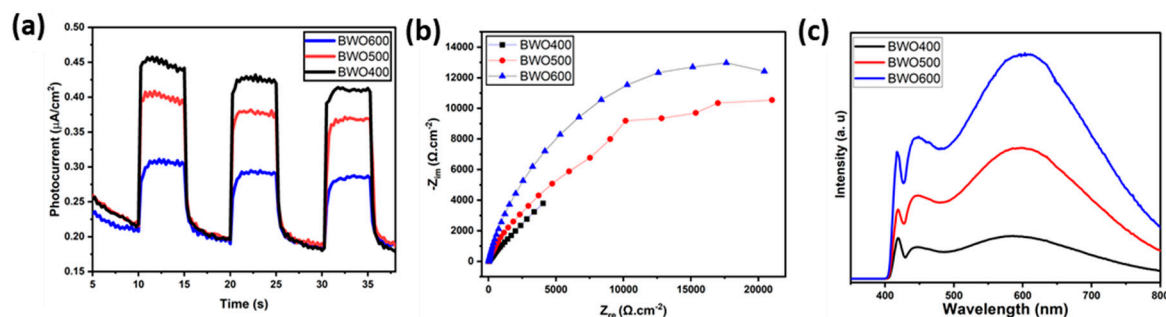

Figure 9. The transient photocurrent curves of BWO400, BWO500, and BWO600 (**a**), EIS Nyquist graphs (**b**) and the photoluminescence PL curves (**c**) of each photocatalyst (BWO400, BWO500, and BWO600).

4.4. Trapping Test

Trapping studies were conducted out to identify the principal oxidizing species that are involved in dye decomposition. Ethylene-Diamine-Tetra-Acetic acid disodium (EDTA), L-ascorbic acid (L-asc), and Isopropyl Alcohol (IPA) were used as specific and appropriate scavengers of the species likely to be responsible for MO and RhB decomposition, i.e., $OH^\bullet$, $O_2^{\bullet-}$ and holes h^+. Figure 10a illustrates the impact of these trapping agents on the photocatalytic performance of the BWO400 photocatalyst with respect to RhB and MO. As can be seen in this figure, the photocatalytic breakdown efficiencies are 97% and 92% for RhB and MO, respectively, in the absence of scavengers. With the addition of L-ascorbic acid, EDTA, and IPA, these efficiencies dropped to 31%, 45%, and 68% for RhB and 38%, 51%, and 74% for MO, respectively. Therefore, it may be deduced at this stage that superoxide $O_2^{\bullet-}$ and holes h^+ are considered to be the principal species responsible for the photodecomposition of MO and RhB, while hydroxyl radicals $OH^\bullet$ are found to play a secondary function in the photocatalytic degradation. These results are similar to those of Wang et al. [63], who reported that $O_2^{\bullet-}$ and h^+ are the major species implicated in process decomposition.
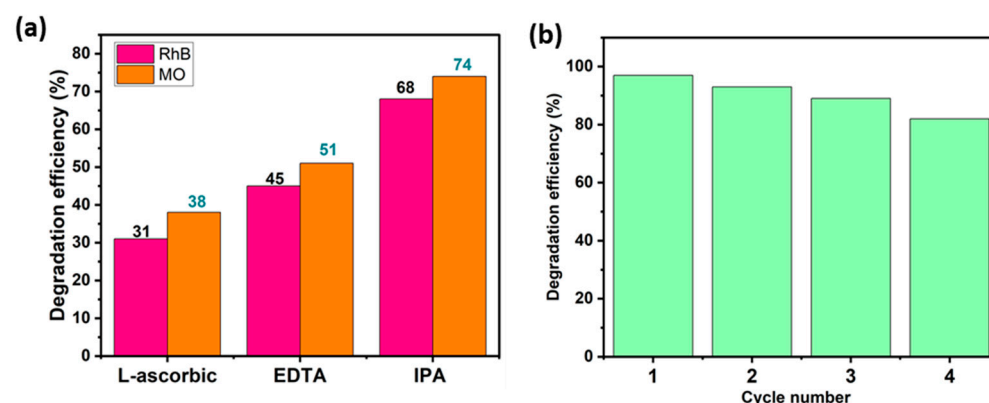

Figure 10. Photocatalytic decomposition efficacy of RhB and MO using BWO400 in the presence of a range of trapping agents (**a**), and the recycling test of the BWO400 photocatalyst (**b**).

4.5. Recyclability

The stability of the BWO400 catalyst was assessed by recycling the material after each photocatalytic reaction. The collected photocatalyst was rinsed and then dried for reuse. The experimental results presented in Figure 10b indicate that only a slight decline in

photocatalytic activity was detected after four consecutive tests. This slight decrease could be due to photocatalyst loss during recycling.

4.6. Proposed Mechanism

To better explain the photocatalytic process, the valence band (VB) and the conduction band (CB) positions of the BWO400 were measured using Mott–Schottky (MS) analysis (Figure 11a). The MS formula is expressed below:
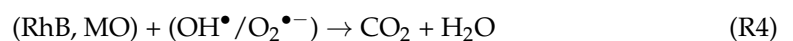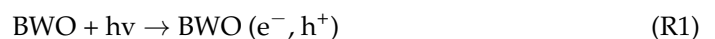
$$C^{-2} = \frac{2}{N_D e \varepsilon \varepsilon_0} \left(V - V_{fb} - \frac{kT}{e} \right) \tag{6}$$

where e, T, K, V_{fb}, V, N_D, ε, ε_0, and C were the electron charge, the absolute temperature, the Boltzmann constant, the flat band potential, the applied potential, the carrier density, the relative permittivity, the permittivity of free space and the space-charge capacitance, respectively. The corresponding curves show a linear variation of $1/C^2$ for greater potentials with a positive slope, which indicates that the prepared BWO400 is an n-type semiconductor (SC). The flat band potential (V_{fb}) deduced from the x-intercept of the MS plots of BWO400 was −0.58 V vs. Ag/AgCl. Based on the recorded potential vs. Ag/AgCl, the normal hydrogen electrode (NHE) potential is calculated as $E_{Ag/AgCl} = E_{NHE} - 0.197$ [63,64]. Generally, the CB potential of n-type SC is more negative by approximately 0.2 V than its V_{fb} [19,58,65]. The band structure of BWO400 photocatalyst can therefore be identified using the following equations:

$$E_{CB} = V_{fb} - 0.2 \tag{7}$$

$$E_g = E_{VB} - E_{CB} \tag{8}$$

Consequently, the value of E_{CB} is found to be −0.78 V vs. Ag/AgCl, which is −0.583 V vs. NHE. The E_{VB} is therefore obtained from the E_{CB} and E_g values and is equal to 2.287 V vs. NHE. To provide more insight about the active species of the BWO400 photocatalyst, we also display the potential of the couple $O_2/O_2^{\bullet-}$ and $H_2O/OH^{\bullet}$, which is −0.33 and 1.99 V vs. NHE, respectively [66]. As shown in Figure 11b, the potential of the VB of BWO is more positive than that of $H_2O/OH^{\bullet}$, while the potential of the CB is more negative with respect to that of $O_2^{\bullet-}/O_2$. Therefore, according to the relative position of the band edges, the BWO400 photocatalyst may readily generate $O_2^{\bullet-}$ and $OH^{\bullet}$ radicals [22,67]. Generally, the photodegradation of the dyes used involves an initial excitation of the Bi_2WO_6 semiconductor (Reaction (1)); excited electrons from the material can be transferred to the CB of the BWO semiconductor. These will react with the oxygen present in the solution to form the reactive species $O_2^{\bullet-}$ (Reaction (2)). The holes in the valence band react with water (H_2O) to form hydroxyl radicals $OH^{\bullet}$ (Reaction (3)). As a result, these reactive species formed ($O_2^{\bullet-}$ and $OH^{\bullet}$) can effectively break down the organic pollutant into CO_2 and H_2O (Reaction (4)) [68]. Table 3 lists the photocatalytic efficiencies of BWO-based catalysts published in the literature, with various tested pollutants and illumination sources. In comparison with the reported photocatalyst in Table 3, the catalyst designed in this research exhibits a high photocatalytic activity compared to other BWO-based photocatalysts.
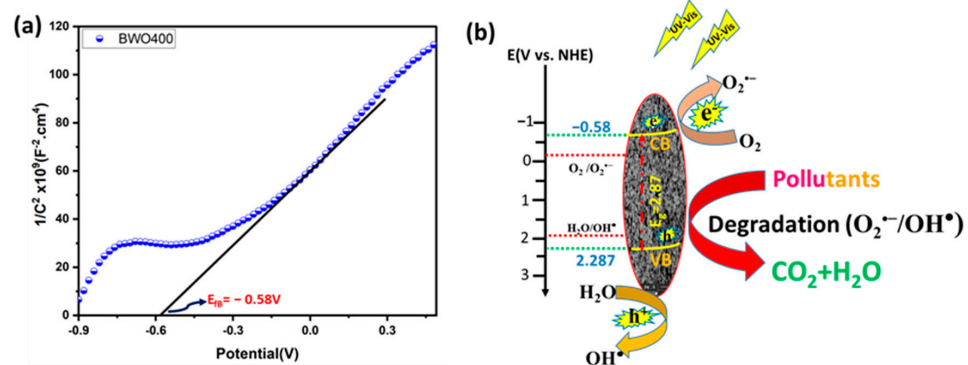
$$BWO + h\nu \rightarrow BWO\,(e^-, h^+) \tag{R1}$$

$$H_2O + h^+ \rightarrow OH^{\bullet} + H^+ \tag{R2}$$

$$O_2 + e^- \rightarrow O_2^{\bullet-} \tag{R3}$$

$$(RhB, MO) + (OH^{\bullet}/O_2^{\bullet-}) \rightarrow CO_2 + H_2O \tag{R4}$$

Figure 11. Mott–Schottky plot of the BWO400 photocatalyst (**a**), and the schematic band structure diagram depicting the proposed degradation mechanism (**b**).

Table 3. A comparative analysis of the photocatalytic efficacy of the BWO photocatalyst with other published photocatalysts.

Photocatalyst	Pollutants	Concentration (mg/L)	Light Source (W)	Efficiency (%)	Ref.
Sb^{3+}/Bi_2WO_6	RhB and MO	6.5	Solar light	80.58 and 77.23	[69]
Bi_2WO_6/WO_3	MO	-	Solar light	75.65	[70]
Bi_2WO_6	RhB	5	500 W Xe	95	[71]
Bi_2WO_6	RhB	5	500 W Xe	92	[72]
$Bi_2WO_6/BiOCl$	MO	10	Xe lamp	68	[73]
$Fe-Bi_2WO_6$	RhB	10	500 W Xe	93	[74]
Bi_2WO_6	RhB	4.8	300 W Xe	90	[75]
BWO400	RhB and MO	5	Philips lamps (300 W)	97 and 92	This study

4.7. Estimation of RhB and MO Mineralization by COD Analysis

The *COD* measurement provides an idea of the degree of mineralization of the contaminant after photocatalytic degradation and offers further information on the photocatalytic activity of the material. Figure 12a,b show the *COD* elimination rates when the BWO400 photocatalyst was used for the decomposition of RhB and MO. Figure 12 shows that as the irradiation time is increased, the *COD* reduction rate rises to 82% and 79% for RhB and MO, respectively, which indicates that mineralization of RhB and MO has occurred through the degradation of dye molecules into CO_2 and H_2O. The remarkable *COD* reductions observed in our study can be due to the specific characteristics of the BWO400 photocatalyst in terms of its morphology and optical and photoelectrochemical properties, whose mechanism of action relies on its capability to capture solar energy to activate catalytic reactions. The successful performance of BWO400 material in reducing *COD* levels demonstrates its potential as a viable material for water treatment applications.
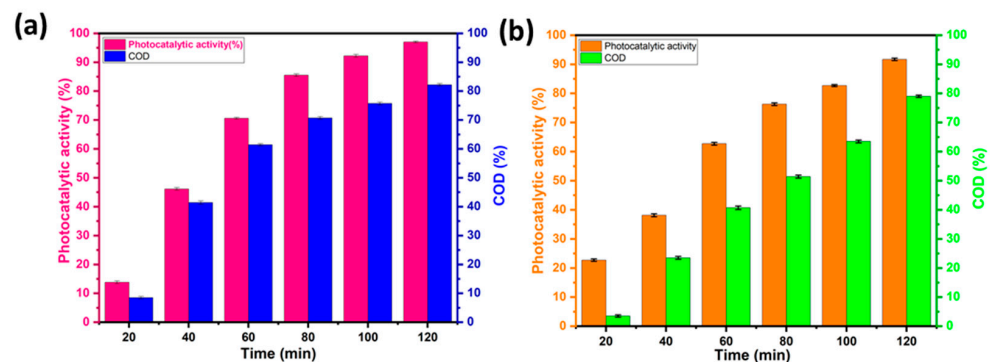

Figure 12. Variation in the chemical oxygen demand (*COD*) removal with the irradiation time for RhB (**a**) and MO (**b**).

5. Conclusions

In the present work, for environmental remediation, Bi_2WO_6 NPs (BWO) photocatalyst was designed by using a chemical precipitation method. Further, the effects of subsequent photocatalyst annealing at 400 °C, 500 °C, and 600 °C for organic dye photodegradation enhancement were investigated. It is shown that the photocatalyst calcination temperature has a profound influence on its morphology, its optical properties, its photoelectrochemical behavior, and its photocatalytic activity. The photocatalyst structural analysis revealed an orthorhombic phase, where the size of the uniform spherical grains increased with the calcination temperature. The BWO nanoparticles annealed at 400 °C demonstrated 97% and 92% elimination of RhB and MO model pollutants in photocatalytic degradation reactions after 2 h solar irradiation. In addition, the BWO annealed at 400 °C showed the highest transient photocurrent density among the studied catalysts along with a stable photoelectrochemical behavior and maintained its photocatalytic activity up to four cycles. The overall data indicate that the superoxide $O_2^{\bullet-}$ and holes h^+ are the major species responsible for the dye photodegradation.

References

1. Channab, B.-E.; Ouardi, M.E.; Layachi, O.A.; Marrane, S.E.; Idrissi, A.E.; BaQais, A.A.; Ahsaine, H.A. Recent Trends on MIL-Fe Metal-Organic Frameworks: Synthesis Approaches, Structural Insights, and Applications in Organic Pollutant Adsorption and Photocatalytic Degradation: A Review. *Environ. Sci. Nano* **2023**, *10*, 2957–2988. [CrossRef]
2. Khanal, V.; Balayeva, N.O.; Günnemann, C.; Mamiyev, Z.; Dillert, R.; Bahnemann, D.W.; Subramanian, V. (Ravi) Photocatalytic NOx Removal Using Tantalum Oxide Nanoparticles: A Benign Pathway. *Appl. Catal. B Environ.* **2021**, *291*, 119974. [CrossRef]
3. Hamou, A.B.; Enneiymy, M.; Farsad, S.; Amjlef, A.; Chaoui, A.; Nouj, N.; Majdoub, A.; Jada, A.; Ez-zahery, M.; Alem, N.E. Novel Chemically Reduced Cobalt-Doped g-C_3N_4 (CoCN-x) as a Highly Heterogeneous Catalyst for the Super-Degradation of Organic Dyes via Peroxymonosulfate Activation. *Mater. Adv.* **2024**. [CrossRef]
4. Farsad, S.; Amjlef, A.; Chaoui, A.; Hamou, A.B.; Hamma, C.; Benafqir, M.; Jada, A.; Alem, N.E. Harnessing Carbon-Based Material from Food Waste Digestate for Dye Adsorption: The Role of Hydrogel Beads in Enhancing Stability and Regenerative Capacity. *Mater. Adv.* **2023**, *4*, 6599–6611. [CrossRef]

5. Farsad, S.; Anfar, Z.; Ait El Fakir, A.; Amjlef, A.; El Alem, N.; Ionel, I. Methane Recovery from the Leachate of Municipal Solid Waste Landfill by Using Anaerobic Digestion. Case Study. In Proceedings of the 30th European Biomass Conference and Exhibition Proceedings, Online, 9–12 May 2022; pp. 223–227. [CrossRef]

6. El Idrissi, A.; Channab, B.; Essamlali, Y.; Zahouily, M. Superabsorbent Hydrogels Based on Natural Polysaccharides: Classification, Synthesis, Physicochemical Properties, and Agronomic Efficacy under Abiotic Stress Conditions: A Review. *Int. J. Biol. Macromol.* **2024**, *258*, 128909. [CrossRef] [PubMed]

7. Channab, B.-E.; El Idrissi, A.; Essamlali, Y.; Zahouily, M. Nanocellulose: Structure, Modification, Biodegradation and Applications in Agriculture as Slow/Controlled Release Fertilizer, Superabsorbent, and Crop Protection: A Review. *J. Environ. Manag.* **2024**, *352*, 119928. [CrossRef] [PubMed]

8. El Ouardi, M.; El aouni, A.; Ahsaine, H.A.; Zbair, M.; BaQais, A.; Saadi, M. ZIF-8 Metal Organic Framework Composites as Hydrogen Evolution Reaction Photocatalyst: A Review of the Current State. *Chemosphere* **2022**, *308*, 136483. [CrossRef]

9. El ouardi, m.; El Idrissi, A.; Arab, M.; Zbair, M.; Haspel, H.; Saadi, M.; Ait Ahsaine, H. Review of Photoelectrochemical Water Splitting: From Quantitative Approaches to Effect of Sacrificial Agents, Oxygen Vacancies, Thermal and Magnetic Field on (Photo)Electrolysis. *Int. J. Hydrogen Energy* **2023**, *51*, 1044–1067. [CrossRef]

10. Chakhtouna, H.; El Allaoui, B.; Zari, N.; Bouhfid, R.; Qaiss, A.e.K. Bio-Inspired Polymers as Organic Electrodes for Batteries. In *Organic Electrodes: Fundamental to Advanced Emerging Applications*; Gupta, R.K., Ed.; Engineering Materials; Springer International Publishing: Cham, Switzerland, 2022; pp. 189–206. ISBN 978-3-030-98021-4.

11. El Allaoui, B.; Benzeid, H.; Zari, N.; Qaiss, A.e.K.; Bouhfid, R. Functional Cellulose-Based Beads for Drug Delivery: Preparation, Functionalization, and Applications. *J. Drug Deliv. Sci. Technol.* **2023**, *88*, 104899. [CrossRef]

12. El Allaoui, B.; Chakhtouna, H.; Zari, N.; Benzeid, H.; Qaiss, A.e.K.; Bouhfid, R. Superhydrophobic Alkylsilane Functionalized Cellulose Beads for Efficient Oil/Water Separation. *J. Water Process Eng.* **2023**, *54*, 104015. [CrossRef]

13. Farsad, S.; Hamou, A.B.; Chaoui, A.; Amjlef, A.; Lhanafi, S.; Et-Taleb, S.; Alem, N.E. Maximizing Bio-Methane Potential from Municipal Landfill Leachate through Ultrasonic Pretreatment. *Heliyon* **2023**, *9*, e21347. [CrossRef]

14. Mazkad, D.; El Idrissi, A.; Marrane, S.E.; Lazar, N.; El Ouardi, M.; Dardari, O.; Channab, B.-E.; Ait Layachi, O.; Farsad, S.; Baqais, A.; et al. An Innovative Diatomite-Polypyrrole Composite for Highly Efficient Cr (VI) Removal through Optimized Adsorption via Surface Response Methodology. *Colloids Surf. Physicochem. Eng. Asp.* **2024**, *685*, 133172. [CrossRef]

15. Marrane, S.E.; Dânoun, K.; Essamlali, Y.; Aboulhrouz, S.; Sair, S.; Amadine, O.; Jioui, I.; Rhihil, A.; Zahouily, M. Fixed-Bed Adsorption of Pb(II) and Cu(II) from Multi-Metal Aqueous Systems onto Cellulose-g-Hydroxyapatite Granules: Optimization Using Response Surface Methodology. *RSC Adv.* **2023**, *13*, 31935–31947. [CrossRef]

16. Amjlef, A.; Farsad, S.; Chaoui, A.; Ben Hamou, A.; Ezzahery, M.; Et-Taleb, S.; El Alem, N. Effective Adsorption of Orange G Dye Using Chitosan Cross-Linked by Glutaraldehyde and Reinforced with Quartz Sand. *Int. J. Biol. Macromol.* **2023**, *239*, 124373. [CrossRef] [PubMed]

17. Marrane, S.E.; Dânoun, K.; Allouss, D.; Sair, S.; Channab, B.-E.; Rhihil, A.; Zahouily, M. A Novel Approach to Prepare Cellulose-g-Hydroxyapatite Originated from Natural Sources as an Efficient Adsorbent for Heavy Metals: Batch Adsorption Optimization via Response Surface Methodology. *ACS Omega* **2022**, *7*, 28076–28092. [CrossRef]

18. Ait Ahsaine, H.; BaQais, A.; Arab, M.; Bakiz, B.; Benlhachemi, A. Synthesis and Electrocatalytic Activity of Bismuth Tungstate Bi2WO6 for Rhodamine B Electro-Oxidation. *Catalysts* **2022**, *12*, 1335. [CrossRef]

19. El Ouardi, M.; Ait Layachi, O.; Amaterz, E.; El Idrissi, A.; Taoufyq, A.; Bakiz, B.; Benlhachemi, A.; Arab, M.; BaQais, A.; Ait Ahsaine, H. Photo-Electrochemical Degradation of Rhodamine B Using Electrodeposited $Mn_3(PO_4)2.3H_2O$ Thin Films. *J. Photochem. Photobiol. Chem.* **2023**, *444*, 115011. [CrossRef]

20. El ouardi, m.; Idrissi, A.; Ahsaine, H.; BaQais, A.; Saadi, M.; Arab, M. Current Advances on Nanostructured Oxide Photoelectro-catalysts for Water Splitting: A Comprehensive Review. *Surf. Interfaces* **2024**, *45*, 103850. [CrossRef]

21. Mazkad, D.; Lazar, N.; Benzaouak, A.; Moussadik, A.; El Habib Hitar, M.; Touach, N.; El Mahi, M.; Lotfi, E.M. Photocatalytic Properties Insight of Sm-Doped $LiNbO_3$ in Ferroelectric $Li_{1-x}NbSm_{1/3x}O_3$ System. *J. Environ. Chem. Eng.* **2023**, *11*, 109732. [CrossRef]

22. Lotfi, S.; El Ouardi, M.; Ait Ahsaine, H.; Madigou, V.; BaQais, A.; Assani, A.; Saadi, M.; Arab, M. Low-Temperature Synthesis, Characterization and Photocatalytic Properties of Lanthanum Vanadate $LaVO_4$. *Heliyon* **2023**, *9*, e17255. [CrossRef]

23. Elaouni, A.; El Ouardi, M.; BaQais, A.; Arab, M.; Saadi, M.; Ahsaine, H.A. Bismuth Tungstate Bi_2WO_6: A Review on Structural, Photophysical and Photocatalytic Properties. *RSC Adv.* **2023**, *13*, 17476–17494. [CrossRef] [PubMed]

24. Jaspal, D.; Malviya, A.; El Allaoui, B.; Zari, N.; Bouhfid, R.; Qaiss, A.e.K.; Bhagwat, S. Emerging Advances of Composite Membranes for Seawater Pre-Treatment: A Review. *Water Sci. Technol.* **2023**, *88*, 408–429. [CrossRef] [PubMed]

25. Channab, B.-E.; Ouardi, M.E.; Marrane, S.E.; Layachi, O.A.; Idrissi, A.E.; Farsad, S.; Mazkad, D.; BaQais, A.; Lasri, M.; Ahsaine, H.A. Alginate@$ZnCO_2O_4$ for Efficient Peroxymonosulfate Activation towards Effective Rhodamine B Degradation: Optimization Using Response Surface Methodology. *RSC Adv.* **2023**, *13*, 20150–20163. [CrossRef]

26. El Allaoui, B.; Benzeid, H.; Zari, N.; Qaiss, A.e.K.; Bouhfid, R. Cellulose Beads Supported $CoFe_2O_4$: A Novel Heterogeneous Catalyst for Efficient Rhodamine B Degradation via Advanced Oxidation Processes. *Int. J. Biol. Macromol.* **2023**, *259*, 128893. [CrossRef] [PubMed]

27. Daskalaki, V.M.; Antoniadou, M.; Li Puma, G.; Kondarides, D.I.; Lianos, P. Solar Light-Responsive Pt/CdS/TiO$_2$ Photocatalysts for Hydrogen Production and Simultaneous Degradation of Inorganic or Organic Sacrificial Agents in Wastewater. *Environ. Sci. Technol.* **2010**, *44*, 7200–7205. [CrossRef] [PubMed]

28. Li, H.; Shi, X.; Liu, X.; Li, X. Synthesis of Novel, Visible-Light Driven S, N-Doped NaTaO$_3$ Catalysts with High Photocatalytic Activity. *Appl. Surf. Sci.* **2020**, *508*, 145306. [CrossRef]

29. Chang, W.K.; Rao, K.K.; Kuo, H.C.; Cai, J.F.; Wong, M.S. A Novel Core–Shell like Composite In$_2$O$_3$@ CaIn$_2$O$_4$ for Efficient Degradation of Methylene Blue by Visible Light. *Appl. Catal. Gen.* **2007**, *321*, 1–6. [CrossRef]

30. Wang, X.; Gu, F.; Li, L.; Fang, G.; Wang, X. A Facile Mixed-Solvothermal Route to γ-Bi$_2$MoO$_6$ Nanoflakes and Their Visible-Light-Responsive Photocatalytic Activity. *Mater. Res. Bull.* **2013**, *48*, 3761–3765. [CrossRef]

31. Shi, B.; Yin, H.; Gong, J.; Nie, Q. A Novel Pn Heterojunction of Ag$_2$O/Bi$_4$Ti$_3$O$_{12}$ Nanosheet with Exposed (0 0 1) Facets for Enhanced Visible-Light-Driven Photocatalytic Activity. *Mater. Lett.* **2017**, *201*, 74–77. [CrossRef]

32. Zhou, L.; Jin, C.; Yu, Y.; Chi, F.; Ran, S.; Lv, Y. Molten Salt Synthesis of Bi2WO6 Powders with Enhanced Visible-Light-Induced Photocatalytic Activities. *J. Alloys Compd.* **2016**, *680*, 301–308. [CrossRef]

33. Ait Ahsaine, H. UV-Light Photocatalytic Properties of the Bismuth Lutetium Tungstate System Bi$_2$-xLuxWO$_6$ (0 ≤ x ≤ 1). *Mater. Lett.* **2020**, *276*, 128221. [CrossRef]

34. Ahsaine, H.A.; Jaouhari, A.E.; Slassi, A.; Ezahri, M.; Benlhachemi, A.; Bakiz, B.; Guinneton, F.; Gavarri, J.-R. Electronic Band Structure and Visible-Light Photocatalytic Activity of Bi$_2$WO$_6$: Elucidating the Effect of Lutetium Doping. *RSC Adv.* **2016**, *6*, 101105–101114. [CrossRef]

35. Lv, N.; Li, Y.; Huang, Z.; Li, T.; Ye, S.; Dionysiou, D.D.; Song, X. Synthesis of GO/TiO$_2$/Bi$_2$WO$_6$ Nanocomposites with Enhanced Visible Light Photocatalytic Degradation of Ethylene. *Appl. Catal. B Environ.* **2019**, *246*, 303–311. [CrossRef]

36. Ait Ahsaine, H.; Ezahri, M.; Benlhachemi, A.; Bakiz, B.; Guinneton, F.; Gavarri, J.-R. Electrical impedance spectroscopy analyses and optical properties of the bismuth lutetium tungstate BiLuWO$_6$. *Ferroelectrics* **2017**, *515*, 112–119. [CrossRef]

37. Ait Ahsaine, H.; Ezahri, M.; Benlhachemi, A.; Bakiz, B.; Villain, S.; Guinneton, F.; Gavarri, J.-R. Novel Lu-doped Bi$_2$WO$_6$ nanosheets: Synthesis, growth mechanisms and enhanced photocatalytic activity under UV-light irradiation. *Ceram. Int.* **2016**, *42*, 8552–8558. [CrossRef]

38. Wang, L.; Guo, C.; Chen, F.; Ning, J.; Zhong, Y.; Hu, Y. pH-Induced Hydrothermal Synthesis of Bi$_2$WO$_6$ Nanoplates with Controlled Crystal Facets for Switching Bifunctional Photocatalytic Water Oxidation/Reduction Activity. *J. Colloid Interface Sci.* **2021**, *602*, 868–879. [CrossRef]

39. Basaleh, A.S.; El-Hout, S.I. Sol-Gel Synthesis of Photoactive PtO/Bi$_2$WO$_6$ Nanocomposites for Improved Photoreduction of Hg (II) Ions under Visible Illumination. *Mol. Catal.* **2023**, *547*, 113413. [CrossRef]

40. Hoang, L.H.; Phu, N.D.; Peng, H.; Chen, X.-B. High Photocatalytic Activity N-Doped Bi$_2$WO$_6$ Nanoparticles Using a Two-Step Microwave-Assisted and Hydrothermal Synthesis. *J. Alloys Compd.* **2018**, *744*, 228–233. [CrossRef]

41. Alfaro, S.O.; Martínez-De La Cruz, A. Synthesis, Characterization and Visible-Light Photocatalytic Properties of Bi$_2$WO$_6$ and Bi$_2$W$_2$O$_9$ Obtained by Co-Precipitation Method. *Appl. Catal. Gen.* **2010**, *383*, 128–133. [CrossRef]

42. Hao, N.; Chen, S.; Qian, J.; Zhang, Y.; Liu, Q.; Zhang, X.; Wang, K. A Sensitive Photoelectrochemical (PEC) Platform Fabricated with Nitrogen-Doped Graphene Quantum Dots Decorated Bi$_2$WO$_6$ for Detection of Pentachlorophenol. *J. Electroanal. Chem.* **2017**, *801*, 410–415. [CrossRef]

43. Al-Harahsheh, M.; Shawabkeh, R.; Al-Harahsheh, A.; Tarawneh, K.; Batiha, M.M. Surface Modification and Characterization of Jordanian Kaolinite: Application for Lead Removal from Aqueous Solutions. *Appl. Surf. Sci.* **2009**, *255*, 8098–8103. [CrossRef]

44. Shi, R.; Huang, G.; Lin, J.; Zhu, Y. Photocatalytic Activity Enhancement for Bi$_2$WO$_6$ by Fluorine Substitution. *J. Phys. Chem. C* **2009**, *113*, 19633–19638. [CrossRef]

45. Zhu, Y.; Wang, Y.; Ling, Q.; Zhu, Y. Enhancement of Full-Spectrum Photocatalytic Activity over BiPO$_4$/Bi$_2$WO$_6$ Composites. *Appl. Catal. B Environ.* **2017**, *200*, 222–229. [CrossRef]

46. Kong, X.Y.; Choo, Y.Y.; Chai, S.P.; Soh, A.K.; Mohamed, A.R. Oxygen Vacancies Induced Bi$_2$WO$_6$ for Realization of Full Solar Spectrum Photocatalytic CO$_2$ Reduction: From UV to NIR Region. *Chem. Commun.* **2016**, *52*, 14242–14245. [CrossRef]

47. Shannon, R.D. Handbook of Chemistry and Physics. *Acta Crystallogr.* **1976**, *32*, 751. [CrossRef]

48. Tauc, J.; Grigorovici, R.; Vancu, A. Optical Properties and Electronic Structure of Amorphous Germanium. *Phys. Status Solidi B* **1966**, *15*, 627–637. [CrossRef]

49. Mahanty, S.; Ghose, J. Preparation and Optical Studies of Polycrystalline Bi$_2$WO$_6$. *Mater. Lett.* **1991**, *11*, 254–256. [CrossRef]

50. Liu, Y.; Wei, B.; Xu, L.; Gao, H.; Zhang, M. Generation of Oxygen Vacancy and OH Radicals: A Comparative Study of Bi$_2$WO$_6$ and Bi$_2$WO$_6$−x Nanoplates. *ChemCatChem* **2015**, *7*, 4076–4084. [CrossRef]

51. Jansi Rani, B.; Ravi, G.; Yuvakkumar, R.; Praveenkumar, M.; Ravichandran, S.; Muthu Mareeswaran, P.; Hong, S.I. Bi$_2$WO$_6$ and FeWO$_4$ Nanocatalysts for the Electrochemical Water Oxidation Process. *ACS Omega* **2019**, *4*, 5241–5253. [CrossRef]

52. Wu, L.; Bi, J.; Li, Z.; Wang, X.; Fu, X. Rapid Preparation of Bi$_2$WO$_6$ Photocatalyst with Nanosheet Morphology via Microwave-Assisted Solvothermal Synthesis. *Catal. Today* **2008**, *131*, 15–20. [CrossRef]

53. Wang, J.; Tang, L.; Zeng, G.; Deng, Y.; Dong, H.; Liu, Y.; Wang, L.; Peng, B.; Zhang, C.; Chen, F. 0D/2D Interface Engineering of Carbon Quantum Dots Modified Bi$_2$WO$_6$ Ultrathin Nanosheets with Enhanced Photoactivity for Full Spectrum Light Utilization and Mechanism Insight. *Appl. Catal. B Environ.* **2018**, *222*, 115–123. [CrossRef]

54. Liang, H.; Sun, H.; Zhu, Y.; Fan, L.; Xu, Q. Bi/Bi$_2$WO$_6$ Plasmonic Composites with Enhanced Photocatalytic Activity for Degradation of Gasphase Toluene. *Catal. Lett.* **2023**, *153*, 559–569. [CrossRef]

55. Huang, Y.; Kang, S.; Yang, Y.; Qin, H.; Ni, Z.; Yang, S.; Li, X. Facile Synthesis of Bi/Bi$_2$WO$_6$ Nanocomposite with Enhanced Photocatalytic Activity under Visible Light. *Appl. Catal. B Environ.* **2016**, *196*, 89–99. [CrossRef]

56. Elaouni, A.; Ouardi, M.E.; Zbair, M.; BaQais, A.; Saadi, M.; Ahsaine, H.A. ZIF-8 Metal Organic Framework Materials as a Superb Platform for the Removal and Photocatalytic Degradation of Organic Pollutants: A Review. *RSC Adv.* **2022**, *12*, 31801–31817. [CrossRef] [PubMed]

57. Bahsaine, K.; Benzeid, H.; El Allaoui, B.; Zari, N.; El Mahdi, M.; Qaiss, A.e.K.; Bouhfid, R. Porous Polyvinyl Fluoride Coated Cellulose Beads for Efficient Removal of Cd(II) from Phosphoric Acid. *Int. J. Biol. Macromol.* **2024**, *254*, 127867. [CrossRef]

58. Yang, Z.; Xia, X.; Shao, L.; Wang, L.; Liu, Y. Efficient Photocatalytic Degradation of Tetracycline under Visible Light by Z-Scheme Ag$_3$PO$_4$/Mixed-Valence MIL-88A(Fe) Heterojunctions: Mechanism Insight, Degradation Pathways and DFT Calculation. *Chem. Eng. J.* **2021**, *410*, 128454. [CrossRef]

59. Azmi, S.; Layachi, O.A.; Ouardi, M.E.; Khoumri, E.M.; Moujib, A.; Brouzi, A.E.; Nohair, M.; Pezzato, L.; Dabala, M. Growth of Cu$_2$ZnSnS$_4$ Thin Film Absorber Layer on Transparent Conductive Oxides and Molybdenum Substrates by Electrodeposition for Photovoltaic Application. *Optik* **2022**, *250*, 168320. [CrossRef]

60. Ait Layachi, O.; Azmi, S.; Moujib, A.; Nohair, M.; Khoumri, E. Investigation of Nucleation and Growth Mechanism of Cu$_2$ZnSnS$_4$ Absorber Layer Electrodeposition on Indium Tin Oxide Coated Glass. *Thin Solid Films* **2023**, *782*, 140019. [CrossRef]

61. Boudouma, A.; Ait Layachi, O.; Hrir, H.; Khoumri, E. A One-Step Electrodeposition Method Was Used to Produce Monoclinic Cu$_2$SnS$_3$ Thin Films for the Development of Solar Cells. *J. Mater. Sci. Mater. Electron.* **2023**, *34*, 1903. [CrossRef]

62. Ganeshbabu, M.; Kannan, N.; Venkatesh, P.S.; Paulraj, G.; Jeganathan, K.; MubarakAli, D. Synthesis and Characterization of BiVO$_4$ Nanoparticles for Environmental Applications. *RSC Adv.* **2020**, *10*, 18315–18322. [CrossRef]

63. Wang, Q.; Qian, X.; Xu, H.; He, G.; Chen, H. Enriched Surface Oxygen Vacancies of Bi$_2$WO$_6$/NH$_2$-MIL-68(In) Z-Scheme Heterojunction with Boosted Visible-Light Photocatalytic Degradation for Levofloxacin: Performance, Degradation Pathway and Mechanism Insight. *Sep. Purif. Technol.* **2023**, *306*, 122577. [CrossRef]

64. Zhou, W.; Jia, J.; Lu, J.; Yang, L.; Hou, D.; Li, G.; Chen, S. Recent Developments of Carbon-Based Electrocatalysts for Hydrogen Evolution Reaction. *Nano Energy* **2016**, *28*, 29–43. [CrossRef]

65. Cai, T.; Zeng, W.; Liu, Y.; Wang, L.; Dong, W.; Chen, H.; Xia, X. A Promising Inorganic-Organic Z-Scheme Photocatalyst Ag$_3$PO$_4$/PDI Supermolecule with Enhanced Photoactivity and Photostability for Environmental Remediation. *Appl. Catal. B Environ.* **2020**, *263*, 118327. [CrossRef]

66. Jiang, Z.; Wan, W.; Li, H.; Yuan, S.; Zhao, H.; Wong, P.K. A Hierarchical Z-Scheme α-Fe$_2$O$_3$/g-C$_3$N$_4$ Hybrid for Enhanced Photocatalytic CO$_2$ Reduction. *Adv. Mater.* **2018**, *30*, 1706108. [CrossRef] [PubMed]

67. Wang, D.; Guo, L.; Zhen, Y.; Yue, L.; Xue, G.; Fu, F. AgBr Quantum Dots Decorated Mesoporous Bi$_2$WO$_6$ Architectures with Enhanced Photocatalytic Activities for Methylene Blue. *J. Mater. Chem. A* **2014**, *2*, 11716–11727. [CrossRef]

68. Lotfi, S.; Ouardi, M.E.; Ahsaine, H.A.; Assani, A. Recent Progress on the Synthesis, Morphology and Photocatalytic Dye Degradation of BiVO$_4$ Photocatalysts: A Review. *Catal. Rev.* **2022**, *66*, 1–45. [CrossRef]

69. Wang, Q.; Li, H.; Yu, X.; Jia, Y.; Chang, Y.; Gao, S. Morphology Regulated Bi$_2$WO$_6$ Nanoparticles on TiO$_2$ Nanotubes by Solvothermal Sb3+ Doping as Effective Photocatalysts for Wastewater Treatment. *Electrochim. Acta* **2020**, *330*, 135167. [CrossRef]

70. Liu, Z.; Wang, Q.; Rong, W.; Jin, R.; Cui, Y.; Gao, S. CTAB Assisted Hydrothermal Preparation of Bi$_2$WO$_6$WO$_3$ Nanosheets on TiO$_2$ Nanotube Arrays for Photoelectrocatalytic Applications. *Sep. Purif. Technol.* **2018**, *200*, 191–197. [CrossRef]

71. Silva, R.M.; Batista Barbosa, D.A.; de Jesus Silva Mendonça, C.; de Oliveira Lima, J.R.; Silva, F.C.; Longo, E.; Maciel, A.P.; de Araujo Paschoal, C.W.; Almeida, M.A.P. Morphological Evolution and Visible Light-Induced Degradation of Rhodamine 6G by Nanocrystalline Bismuth Tungstate Prepared Using a Template-Based Approach. *J. Phys. Chem. Solids* **2016**, *96–97*, 83–91. [CrossRef]

72. Shang, Y.; Cui, Y.; Shi, R.; Yang, P. Effect of Acetic Acid on Morphology of Bi$_2$WO$_6$ with Enhanced Photocatalytic Activity. *Mater. Sci. Semicond. Process.* **2019**, *89*, 240–249. [CrossRef]

73. Tahmasebi, N.; Maleki, Z.; Farahnak, P. Enhanced Photocatalytic Activities of Bi$_2$WO$_6$/BiOCl Composite Synthesized by One-Step Hydrothermal Method with the Assistance of HCl. *Mater. Sci. Semicond. Process.* **2019**, *89*, 32–40. [CrossRef]

74. Hu, T.; Li, H.; Du, N.; Hou, W. Iron-Doped Bismuth Tungstate with an Excellent Photocatalytic Performance. *ChemCatChem* **2018**, *10*, 3040–3048. [CrossRef]

75. Phu, N.D.; Hoang, L.H.; Chen, X.-B.; Kong, M.-H.; Wen, H.-C.; Chou, W.C. Study of Photocatalytic Activities of Bi$_2$WO$_6$ Nanoparticles Synthesized by Fast Microwave-Assisted Method. *J. Alloys Compd.* **2015**, *647*, 123–128. [CrossRef]